Passive Microwave Remote Sensing of Rainfall with SSM/I: Algorithm Development and Implementation

JAMES G. FERRIDAY

Colorado Center for Astrodynamics Research, Department of Aerospace Engineering Sciences, University of Colorado, Boulder, Colorado

SUSAN K. AVERY

Department of Electrical Engineering and Cooperative Institute for Research in Environmental Sciences, University of Colorado, Boulder, Colorado

(Manuscript received 30 July 1993, in final form 30 April 1994)

ABSTRACT

A physically based algorithm sensitive to emission and scattering is used to estimate rainfall using the Special Sensor Microwave/Imager (SSM/I). The algorithm is derived from radiative transfer calculations through an atmospheric cloud model specifying vertical distributions of ice and liquid hydrometeors as a function of rain rate. The algorithm is structured in two parts: SSM/I brightness temperatures are screened to detect rainfall and are then used in a rain-rate calculation. The screening process distinguishes between nonraining background conditions and emission and scattering associated with hydrometeors. Thermometric temperature and polarization thresholds determined from the radiative transfer calculations are used to detect rain, whereas the rain-rate calculation is based on a linear function fit to a linear combination of channels. Separate calculations for ocean and land account for different background conditions. The rain-rate calculation is constructed to respond to both emission and scattering, reduce extraneous atmospheric and surface effects, and to correct for beam filling. The resulting SSM/I rain-rate estimates are compared to three precipitation radars as well as to a dynamically simulated rainfall event. Global estimates from the SSM/I algorithm are also compared to continental and shipboard measurements over a 4-month period. The algorithm is found to accurately describe both localized instantaneous rainfall events and global monthly patterns over both land and ocean. Over land the 4-month mean difference between SSM/I and the Global Precipitation Climatology Center continental rain gauge database is less than 10%. Over the ocean, the mean difference between SSM/I and the Legates and Willmott global shipboard rain gauge climatology is less than 20%.

1. Introduction

Rainfall plays a critical role in the global energy and hydrologic cycles. The amount and distribution of rainfall drives the general atmospheric circulation, modifies the ocean surface layer, and controls the terrestrial biological system. To monitor global rainfall, an algorithm is described for use with the Special Sensor Microwave/Imager (SSM/I), the latest multichannel passive microwave radiometer in operational deployment. Rainfall estimates from SSM/I have been shown to compare favorably with ground-based observations; however, continued algorithm development is needed to further reduce rainfall estimation errors (Adler et al. 1993; Berg and Chase 1992; Grody 1991; Liu and Curry 1992; Spencer et al. 1989).

Recent intercomparisons of current SSM/I rainfall algorithms reveal significant differences in rainfall estimates (Lee et al. 1991). These differences result from a variety of theoretical approaches utilized in algorithm development. There are differences in treating the attenuation and scattering in the signal, separating rainfall response from surface variability, accounting for rainfall inhomogeneity in the radiometer field of view, and distinguishing between warm rain events and nonprecipitating cloud liquid water. In support of the need for readily available rainfall estimation algorithms for intercomparisons, an SSM/I rainfall algorithm is described here that is theoretically based, simple in form, and compares favorably with surface observations.

2. Passive microwave theory

a. Cloud model

Passive microwave rainfall remote sensing is based on an understanding of the effects of rainfall on upwelling radiances measurable by a spaceborne radiometer. The development of the SSM/I rainfall algorithm begins with a description of microwave radiative transfer theory applied to a physical model detailing

Corresponding author address: Dr. James G. Ferriday, University of Colorado, CCAR Campus Box 431, Boulder, CO 80309-0431.
E-mail: ferriday@boulder.colorado.edu

both the underlying surface and atmospheric conditions. The cloud model specifies the amount and distribution of atmospheric and surface components that strongly influence upwelling microwave radiance. Water vapor and molecular oxygen require only a path-integrated specification, whereas liquid and ice hydrometeors, cloud liquid water, and temperature depend on the vertical distribution. Underlying surface parameters such as temperature and emissivity are coupled to the atmospheric parameters to form a cloud model system. Theoretical calculations of radiances upwelling through the model form the basis of estimating the underlying rain rate using actual satellite brightness temperature measurements.

In general, cloud models specify either a plane-parallel, horizontally infinite composition or a vertically structured, horizontally finite cloud distribution. There are two basic approaches for modeling horizontally infinite, plane-parallel clouds. In one basic modeling approach, rain is constrained to below the freezing level and ice to above the freezing level (Spencer et al. 1983). In a more realistic approach, vertical layers containing mixed distributions of rain, cloud liquid water, and ice particles are modeled (Wu and Weinman 1984; Liu and Curry 1992). In more complicated models, numerous atmospheric profiles representing different rain event types are used in a retrieval scheme (Kummerow et al. 1989).

The cloud model used in this study is a vertically structured, plane-parallel, horizontally infinite representation of a raining atmosphere similar to Wu and Weinman (1984) and Liu and Curry (1992). Vertical hydrometeor profiles, including raindrops, ice particles, and cloud liquid water are specified from 0 to 14 km in a series of homogeneous layers. The model represents rain cloud conditions typical of stratiform rain at low rain rates and convective rain at higher rain rates. Raindrops are found exclusively below the freezing level for low rain rates, but as rain rate increases, raindrops are included in layers above the freezing level. Ice particles, modeled as oblate frozen drops, are distributed above the freezing level. Ice content increases dramatically at high rain rates, a condition representative of convective storms.

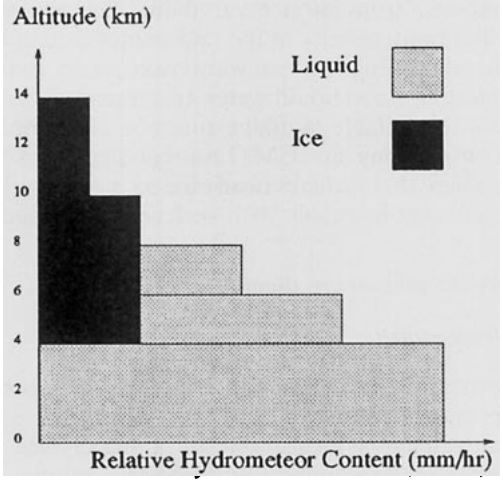

FIG. 1. Modeled liquid and ice phase hydrometeor contents, normalized by surface rain rate, and distributed through altitude.

TABLE 1. Parameters used in the cloud model for theoretical radiative transfer calculations.

Surface temperature	288 K
Land emissivity	0.95
Humidity	90%
Lapse rate	6.5 K km^{-1}
Maximum cloud height	14 km
Cloud liquid water	0–0.2 g m^{-3}
Space background	2.7 K

The distribution of hydrometeors within each layer is shown for liquid and ice in Fig. 1. The rain rate is constant from the surface to 4 km. A layer of cloud liquid water is also included from 4 to 6 km. Ice and supercooled water drops compose mixed layers between 4 and 8 km. The rain rate decreases while ice increases linearly with altitude in this mixed layer. Ice content at 8 km is one-half the surface rain rate, and above 8 km, decreases linearly with height. The cloud-top height increases linearly with surface rain rate from 8 to 12 km.

Table 1 lists the parameters used in the model that are independent of rain rate. The temperature profile has a freezing level at 4 km and a lapse rate of 6.5 K km^{-1}, corresponding to pseudoadiabatic conditions. Humidity is held constant at 90% through all layers. The model includes cloud liquid water with an average content ranging from 0 0.2 g m^{-3} near and below the freezing level. The boundary conditions include a contribution of downwelling radiation from space of 2.7 K and a constant surface temperature of 288 K. The emissivity of the land surface is held constant at 0.95, whereas the ocean surface emissivity is calculated based on an obliquely viewed specular surface.

b. Radiative transfer theory

Equations that describe the theoretical transfer of microwave radiances through a horizontally infinite, plane-parallel vertically structured atmosphere form the basis for calculations of upwelling radiances measurable by SSM/I. The basic equation for the differential radiant intensity can be written as

$$-\mu \frac{dI(\tau, \mu)}{d\tau} = -I(\tau, \mu) + J(\tau, \mu), \qquad (1)$$

where $I(\tau, \mu)$ is the radiant intensity at optical depth τ and $\mu = \cos(\theta)$, where θ is the zenith angle. The source function J is defined as

$$J(\tau, \mu) = [1 - \alpha(\tau)]B(\tau) + \frac{\alpha(\tau)}{2}\int_0^{2\pi} p(\tau, \mu; \mu')I(\tau, \mu')d\mu', \quad (2)$$

in which $B(\tau)$ is the Planck function, α is the single-scattering albedo, and p is the single-scattering phase function. The equation for τ, the extinction optical depth at any point in the medium is

$$\tau(z) = \int_z^{z^*} k_{\text{ext}}(z')dz', \quad (3)$$

where k_{ext} is the extinction coefficient, z^* is the cloud-top altitude, and z is the altitude in kilometers (Olson 1989).

The radiant intensity can be expressed in more conventional units as the brightness temperature, which is the thermodynamic temperature of a blackbody emitting an equivalent intensity. At microwave frequencies the Rayleigh–Jeans approximation replaces the Planck function (Liou 1980) for blackbody emission,

$$B_\nu(T) = \left(\frac{2k_{\text{Boltz}}\nu^2}{c^2}\right)T, \quad (4)$$

where T is the thermodynamic temperature of the blackbody, c is the speed of light, ν is the radiation frequency, and k_{Boltz} is the Boltzman constant (1.38×10^{16} erg K^{-1}). The brightness temperature as a function of intensity is then

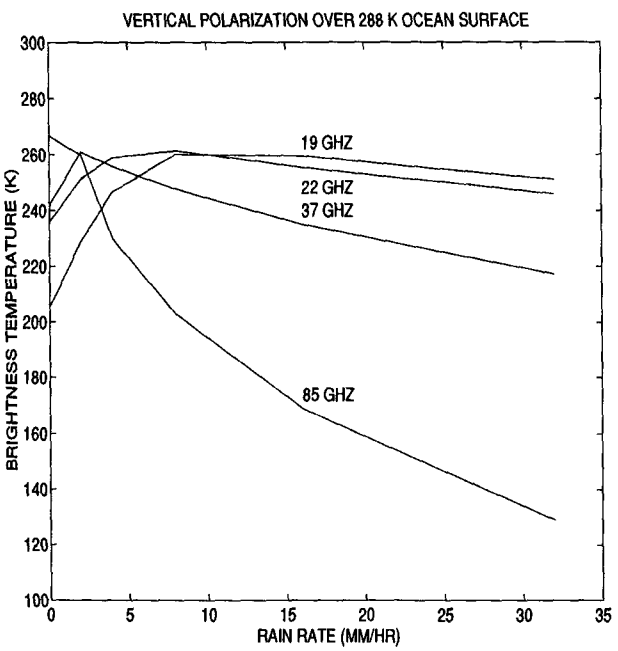

FIG. 2. Theoretical vertically polarized brightness temperatures as a function of cloud model rain rate over the ocean.

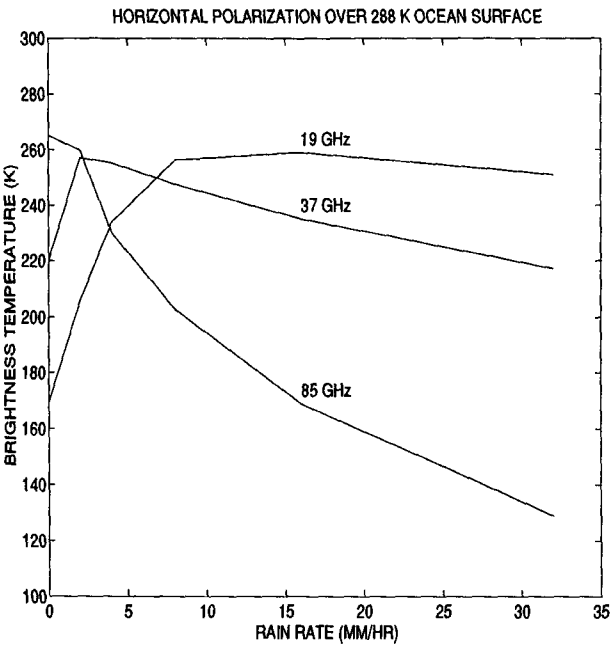

FIG. 3. Theoretical horizontally polarized brightness temperatures as a function of cloud model rain rate over the ocean.

$$T_b = \left(\frac{c^2}{2k_{\text{Boltz}}\nu^2}\right)I. \quad (5)$$

c. *Calculations of upwelling microwave radiances*

Theoretical upwelling brightness temperatures for SSM/I channels are calculated as a function of rain rate. A complete description of the SSM/I instrument may be found in Hollinger (1987). Radiative transfer calculations are made using a one-dimensional Eddington approximation (Kummerow et al. 1989). Brightness temperatures are calculated separately over ocean and land surfaces. In Fig. 2, vertically polarized brightness temperatures are plotted as a function of rain rate over the ocean. Horizontally polarized ocean brightness temperatures are shown in Fig. 3, and vertically polarized brightness temperatures over land are shown in Fig. 4. The form of the curves represents contributions from both emission and scattering associated with liquid and frozen hydrometeors. For a nonraining case, the temperatures are dependent primarily on surface emission.

The relationship between brightness temperature T_b and rain rate RR over ocean includes a marked increase of the lower frequency T_b with rain rate until a saturation temperature is reached. The saturation is followed by a slight decrease in T_b with further rain-rate increases. The initial T_b increase is due to absorption and emission by liquid raindrops, which levels off when the drop layers become optically thick. Contributions

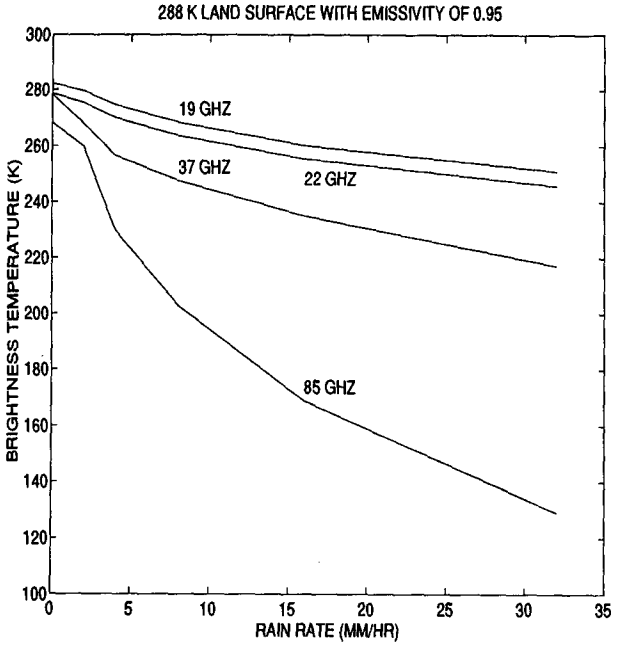

FIG. 4. Theoretical brightness temperatures as a function of rain rate over land.

from scattering by ice aloft and emission from colder drops at higher altitudes depress temperatures at the highest rain rates. The 19-GHz signal is highly polarized at low rain rates due to the specular ocean surface viewed at an oblique angle. The signal becomes unpolarized at high rain rates because of the randomly polarized attenuation produced by raindrops and scattering by ice.

At 85 GHz, the T_b exhibit a pronounced depression beginning at low rain rates, which continues without saturation to rain rates of 35 mm h^{-1}. The no-rain T_b are higher than those from the lower-frequency channels because the emissivity of the ocean surface increases with frequency in this regime. The marked drop in T_b with rain rate at 85 GHz is due primarily to significant scattering by ice hydrometeors above the freezing level in raining clouds. Not all rain clouds contain ice, especially stratiform systems, so the model used in this study contains appreciable ice only at higher rain rates. The 85-GHz channels are less polarized than lower-frequency channels because polarization decreases with frequency for an obliquely viewed ocean surface. The attenuation of T_b with rain rate at 37 GHz contains a mixture of the characteristics outlined for 19 and 85 GHz. At low rain rates the T_b increase is due to raindrop emission, but at higher rain rates the signal is depressed by scattering from ice particles.

The calculations of T_b upwelling over land, which is treated as a Lambertian emitter (Liou 1980), are shown in Fig. 4. The land surface emissions are more variable and less frequency dependent than for the ocean surface. Since the signal is usually effectively unpolarized, only the vertical polarization T_b are calculated. Because the land background appears bright, emission effects at lower frequencies associated with low rain rates are masked. The primary effect of increasing rain rates is to decrease T_b at all channels, but as with ocean signals, scattering is most pronounced at 85 GHz. The scattering signal does not saturate even at a rain rate of 35 mm h^{-1}.

3. Rainfall estimation using SSM/I

a. Algorithm formulation

Based on the theoretical brightness temperatures calculated as a function of rain rate, an algorithm is derived from combinations of SSM/I channels for estimating instantaneous rain rates over both land and ocean. An algorithm is sought that will respond consistently to both low and high rain rates for a variety of rain cloud systems over the highly variable earth background. A further requirement is that the relationship between the algorithm response and rain rate be highly linear to reduce the beam-filling errors resulting from inhomogeneous rain rates filling the satellite instantaneous field of view.

Separate formulations are constructed for ocean and land backgrounds because they have such dissimilar T_b signatures. To utilize information available from the polarization and emission effects at low rain rates, the ocean algorithm is based on polarization differencing and mixed emission-scattering response. Over land, the algorithm relies primarily on scattering information because the signal is usually unpolarized and the warm land background obscures hydrometeor emission. Channel combinations sensitive to low rain rates are chosen to aid in rain thresholding. Also, by adding and subtracting equal numbers of channels, the surface and atmospheric biases introduced by changing climatic regions are reduced. Finally, channels are combined so that they vary nearly linearly with rain rate to reduce the underestimation associated with beam filling.

b. Rain screening

Prior to a rain-rate calculation, the algorithm tests the SSM/I data to distinguish between possible raining events and underlying surface and atmospheric conditions exhibiting an erroneous rainfall signature. Surfaces such as ice, snow, sand, cold ground, and moist soil exhibit signatures similar to rainfall (Grody 1991). Variations in atmospheric water vapor, cloud liquid water, nonprecipitating ice, and temperature profiles produce attenuation and scattering that also may resemble the effects of rainfall (Wilheit 1986). Each of the nonraining conditions may be distinguished from

rain using a testing logic based on separate scattering, attenuation, and polarization criteria.

Over land, the data are flagged as nonraining cold or ice/snow-covered ground if the 19-GHz T_b is less than 255 K. Also over land, if the polarization difference at 37 or 19 GHz is greater than 10 K then the pixel is flagged as desert or moist or flooded soil. These tests are determined from the theoretical brightness temperature response curves by noting the T_b and polarization for low rain-rate thresholds. Over ocean, the polarization difference at 19 GHz must be below 60 K to signal the possible presence of rain. The rain-rate calculation, outlined in the next section, tests for the combined presence of emission and scattering associated with hydrometeors. Because it is thought possible to distinguish between raining and nonraining pixels in most cases over a multitude of different surfaces, flagged pixels in this algorithm are set to zero rain rate rather than left indeterminate.

c. *Rain-rate calculation*

Over ocean, the channel combination chosen to form the core of the rain-rate retrieval algorithm is (19H + 19V + 37H − 22V − 37V − 85H), where the notation describes the frequency and polarization of the SSM/I channel. The basis for this selection, in addition to satisfying the requirements above, lies in the sensitive response of the low-frequency horizontally polarized channels to low rain rates and the depolarization accompanying attenuation by liquid and scattering by ice. A further attribute is that whereas the lower frequencies increase primarily for low rain rates, at high rain rates the higher frequencies continue to decrease when the low frequencies have saturated, so that the algorithm is extended in dynamic range.

The channel combination used for the calculation of land surface rain rates is [19H + 37H − 2(85H)]. The use of only one polarization over land minimizes the effect of surface moisture variations. Since the no-rain signal is already depolarized in most cases and polarizing effects from nonspherical hydrometeors are not modeled, polarization information over land is limited to screening nonraining surfaces such as ice and moist soil. Subtracting the higher-frequency channels from the low-frequency channels gives a nearly linear channel combination dependence on rain rate.

Using the brightness temperatures calculated from the combination of channels selected for the algorithms, a threshold is chosen to signal the presence of rain. There is a trade-off between lowering the threshold to allow sensitivity at lower rain rates, and raising the threshold to adequately screen out nonraining cases. In the ocean algorithm, thresholding between nonprecipitating clouds containing significant amounts of cloud liquid water, and cases where raindrops are actually reaching the ground, is especially difficult. A bias is added to the brightness temperatures such that the threshold is at a rain rate of 0.5 mm h^{-1}. The bias for the ocean algorithm is 170.2 K. The bias for the land algorithm is −15.6 K.

Although the channel differencing utilized in the algorithm formulation will reduce background variations, the effect of surface temperature on the threshold bias is examined. The threshold bias over land depends slightly on surface temperature, exhibiting a range of 37.3 K for surfaces from 273 to 300 K. Therefore, a latitudinally and seasonally varying bias temperature is added to the algorithm over land. The correction is derived from climatological global surface temperatures. The land surface threshold bias becomes $-15.6 + (X/5)$, where X is the absolute value of latitude plus season offset. The season offset is 20 during December, January, and February; −20 during June, July, and August; and 0 for the remaining months. The modeled errors for the ocean estimates are found to vary by less than 1 mm h^{-1} over a surface temperature range from 273 to 300 K, so no latitudinal correction is applied.

Inhomogeneous distributions of rain rates within a satellite instantaneous field of view (IFOV) can cause an underestimation in uncorrected retrieval algorithms developed from idealized rain distributions (Chiu et al. 1990). The underestimation, known as beam-filling errors, results from an inhomogeneously filled IFOV because there is a nonlinear relationship between brightness temperature and rain rate especially at lower frequencies. When an ensemble of T_b contributions from a distribution of rain rates are averaged together in one satellite measurement, the apparent T_b as calculated from a model of homogeneous rates indicates a lower rain rate than the true value (Ferriday and Kummerow 1992). Beam-filling errors contribute to an underestimation of about a factor of 2 when direct emission-based inversion techniques are used for satellite microwave retrievals with a resolution near that of the SSM/I. To correct for the beam-filling error, the T_b combinations are adjusted so that for rain rates below 20 mm h^{-1} the retrieved rain rate will be twice the value predicted by the theoretical radiative transfer calculations.

A regression line is fit to the bias and beam-filling-corrected brightness temperatures to create an inversion formula for converting T_b to rain rates. Over ocean the slope is 18.3 K and over land the slope is 9.1 K. The T_b and regression lines are plotted in Figs. 5 and 6 for ocean and land, respectively. The straight line fit to the T_b preserves simplicity in algorithm implementation and in future modifications if, for example, slope and bias corrections are obtained from comparisons with alternative rain-rate retrievals.

4. Algorithm implementation

a. *Comparison to a dynamical cloud model*

The rainfall algorithm is applied to simulated SSM/I T_b upwelling from a dynamic cloud model. A

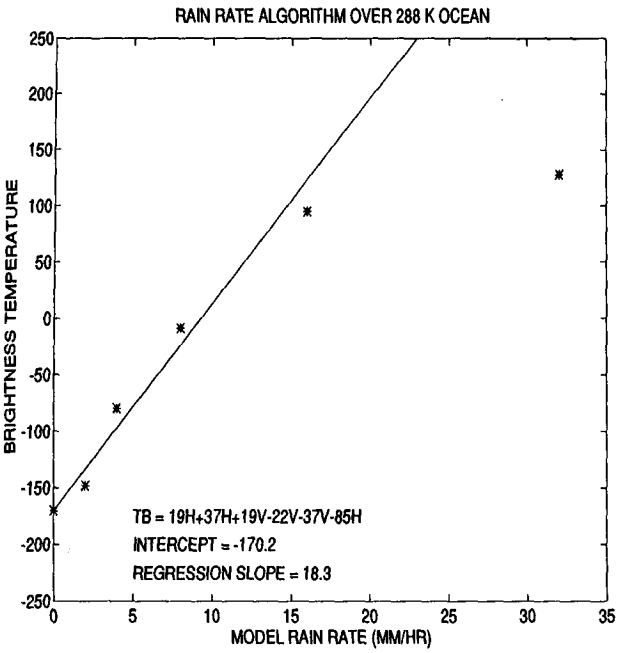

FIG. 5. Formulation of the SSM/I oceanic rain-rate algorithm including the threshold bias-adjusted T_b combination and linear fit versus cloud model rain rate.

fast-moving squall line is simulated by a three-dimensional ensemble cloud system with parameterized microphysics (Tao et al. 1987). The model surface rain rates and upwelling brightness temperatures are averaged into the SSM/I all-channel footprint of 25-km diameter and a comparison is made of estimated and modeled rain rates. In Fig. 7, the SSM/I estimates derived from the algorithm are plotted against the model surface rain rates. The retrieved rain rates are virtually identical to the model surface rain rates with a slope and correlation near unity and a bias near zero. The algorithm senses both the light rainfall near 1 mm h^{-1} and the relatively high rain rates of 20 mm h^{-1}. The model is representative of a realistic storm; however, because the T_b utilized in the retrieval are calculated theoretically by a radiative transfer model, the model- and algorithm-estimated rain rates cannot be considered uncoupled. The results do support the use of the linear fit to the T_b combinations forming the temperature inversion technique.

b. Comparison with surface radar

The ocean and land algorithms are compared with surface radar rain measurements. Radar data are used from three climatologically distinct stations: Darwin, Australia; Cape Canaveral, Florida; and Oklahoma City, Oklahoma. The radar data, part of the Atmospheric and Oceanographic Information Processing System (AOIPS) at NASA/Goddard Space Flight Center, are C- and S-band Doppler radars with 5- and 10-cm wavelengths. The radar resolution, initially reported at 1 km, is collocated in time and space with SSM/I pixels and averaged to match the SSM/I all-channel footprint. The range is bounded by 20 and 180 km to reduce ground clutter and range errors. The radar data were provided with rain rate in millimeters per hour after calibration by appropriate Z–R relationships. The Darwin radar data were collected at 2118 UTC 21 August 1988, the Florida radar data were collected at 2344 UTC 11 December 1988, and the Oklahoma radar data were collected at 0120 UTC 13 July 1987. A full scan from each radar is utilized in a direct comparison of instantaneous rain estimates with the SSM/I algorithm.

The coincident SSM/I and radar data are displayed in Figs. 8, 9, and 10 for Darwin, Cape Canaveral, and Oklahoma, respectively. In all cases the absolute difference between the totals for the SSM/I and radar estimates is less than the radar mean rain rate. The differences between the radar and SSM/I are probably due to a combination of the effects of coastline pixels, satellite misnavigation, and instrument viewing geometry. The Darwin radar scan encompasses a great deal of coastline that is not excluded because the resulting data points would be too few. The SSM/I navigation errors are known to typically reach 10 km and are possibly the cause of the displacement of the squall line in the Oklahoma comparison. The radar estimates of rain rate by the far side of clouds may be adversely influenced by the intermediate cloud attenuation through the storm. Likewise, the SSM/I brightness

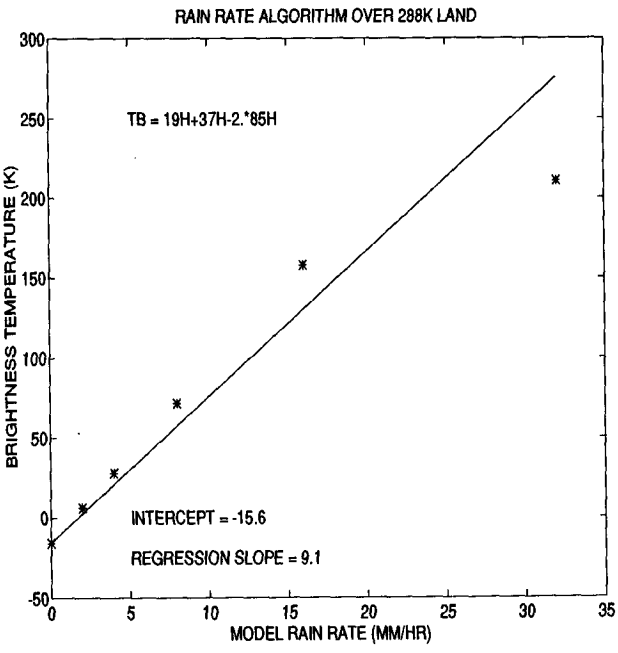

FIG. 6. Formulation of the SSM/I land rain-rate algorithm including the threshold bias-adjusted T_b combination and linear fit versus model rain rate.

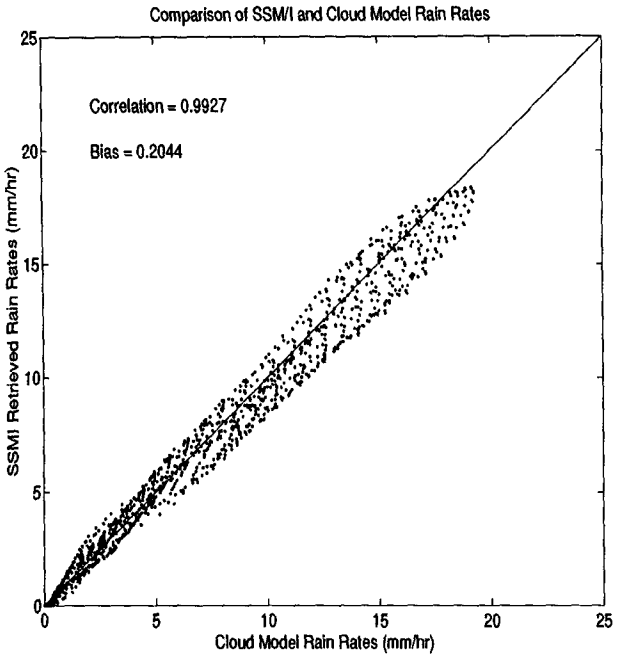

FIG. 7. A comparison of surface rain rates from the Goddard Cumulus Ensemble Model (GCEM) with rain rates estimated by the application of the SSM/I algorithm to brightness temperatures simulated through the model.

temperatures from the lowest layers of heavy storms are, in some cases, completely obscured by the higher layers (Smith and Mugnai 1988). Histograms for each radar comparison and for the combined data, in Fig. 11, show that in each case the majority of the rain rates for both radar and satellite are near 0 mm h^{-1} with decreasing frequency to a limit near 20 mm h^{-1}. The distribution of the Oklahoma rain rates has a lognormal shape, whereas the others are logarithmically decreasing with rain rate. In all three cases the algorithm detects an appropriate rain area and then estimates a reasonable rain rate.

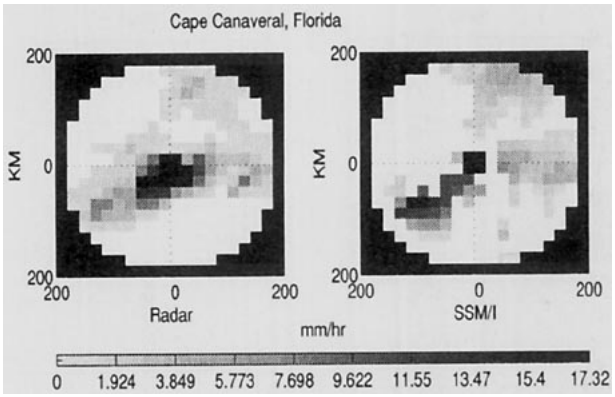

FIG. 9. Coincident rain rates estimated from SSM/I and the Cape Canaveral, Florida, precipitation radar for 2344 UTC 11 December 1988.

c. *Global monthly rain gauge comparison*

The algorithm is applied to four complete months of SSM/I data for August through November 1987. Total precipitation is calculated globally at 1° resolution between +60° and −60° latitude with the exception of coastlines. The SSM/I results are compared with the Global Precipitation Climatology Center (GPCC) (GPCC 1992) rain gauge dataset over land and a shipboard rain gauge climatology by Legates and Willmott (1990) (LW) over oceans. The GPCC dataset is compiled from measurements taken over the same time period as the SSM/I data, whereas the LW represents the climatology for the 4-month period. The 4-month precipitation totals are paired at 1° resolution and a statistical comparison is conducted.

The GPCC and SSM/I continental comparison results are listed in Table 2. The mean SSM/I value is 240.8 mm and the mean GPCC value is 222.0 mm yielding a mean difference of 18.7 mm. The mean of the absolute difference between grid cell pairs is 155.1

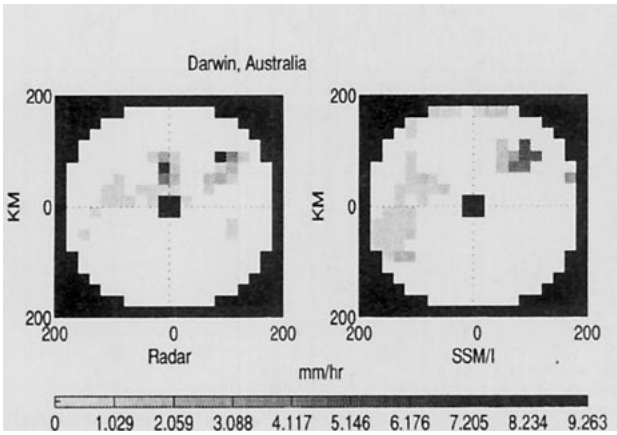

FIG. 8. Coincident rain rates estimated from SSM/I and the Darwin, Australia, precipitation radar for 2118 UTC 21 August 1988.

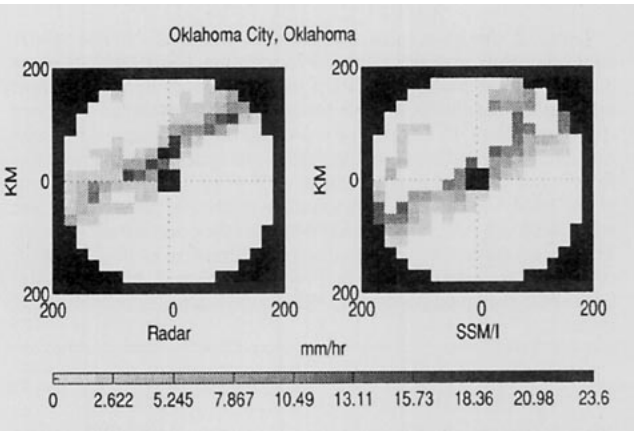

FIG. 10. Coincident rain rates estimated from SSM/I and the Oklahoma City, Oklahoma, precipitation radar for 0120 UTC 13 July 1987.

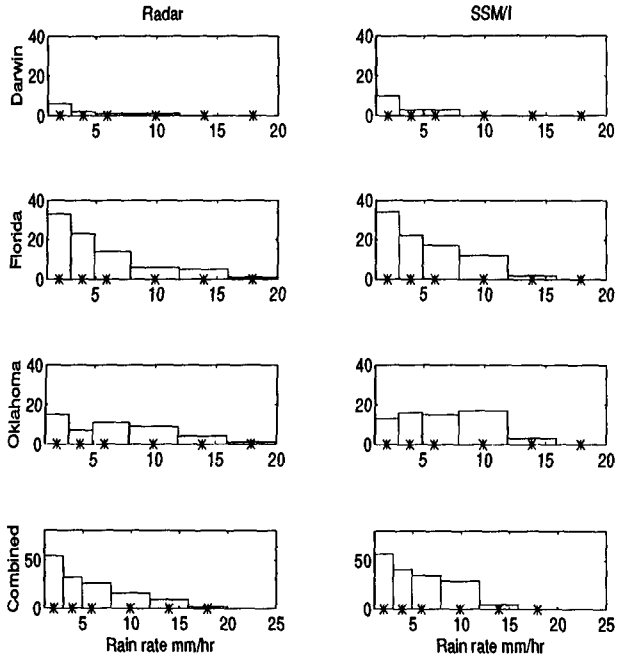

FIG. 11. Rain-rate distributions from precipitation radars at Darwin, Australia; Cape Canaveral, Florida; and Oklahoma City, Oklahoma; with estimates from coincident SSM/I overpasses. The radar rain rates are spatially averaged to match the SSM/I all-channel resolution and the land SSM/I rain-rate algorithm is applied to pixels that include coastline.

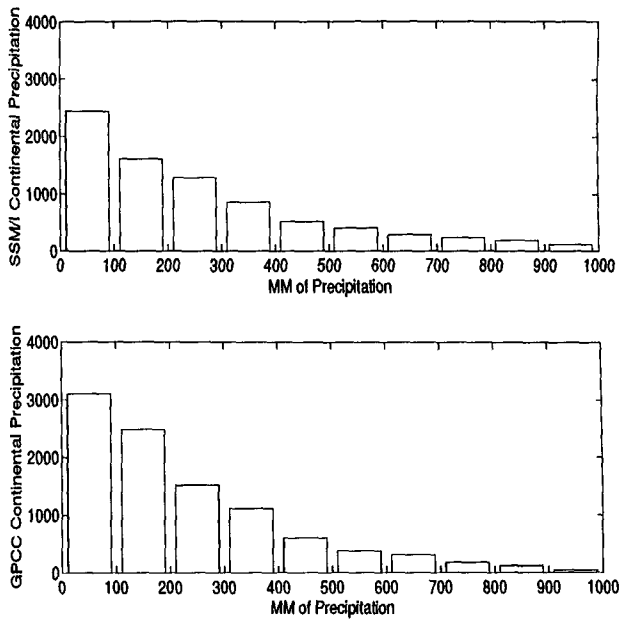

FIG. 12. Distributions of total global continental precipitation for August through November 1987 from estimates by the SSM/I algorithm and a rain gauge areal average by the GPCC.

mm and the correlation of the totals is 0.70. Because of the differences in temporal and spatial sampling characteristics between the SSM/I and rain gauges, the absolute differences will be much higher than the difference of the mean. The satellite will typically provide one or two overpasses each day, which undersamples in time, whereas the GPCC typically contains cells with one or two gauges, which undersamples in space.

Histograms of the distribution of rainfall totals for GPCC and SSM/I are shown in Fig. 12. The GPCC contains more grid cells with totals from 0 to 200 mm and the SSM/I contains slightly more cells with totals between 300 and 1000 mm. The distribution of the precipitation totals suggests that the SSM/I algorithm is providing accurate totals over relatively dry continental areas as well as areas with persistent convective activity. The spatial distribution of rainfall is further

TABLE 2. Statistics calculated from a comparison of the SSM/I land algorithm and the Global Precipitation Climatology Center (GPCC) continental precipitation database. Monthly precipitation totals at 1° resolution for the period August–November 1987 are compared. The GPCC database represents areal-averaged rain gauge measurements. Statistics are calculated from matching each grid point from −180° to 180° longitude and −60° to 60° latitude. The mean of the SSM/I and GPCC precipitation totals are calculated as the mean of all reported values including zeroes over continental surfaces. The mean difference, mean absolute difference, and correlation coefficient are calculated by pairing corresponding gridded SSM/I and GPCC precipitation totals for all reported values over continental surfaces.

SSM/I mean	240.8 mm
GPCC mean	222.0 mm
Mean difference	18.7 mm
Mean absolute difference	155.1 mm
Correlation coefficient	0.70

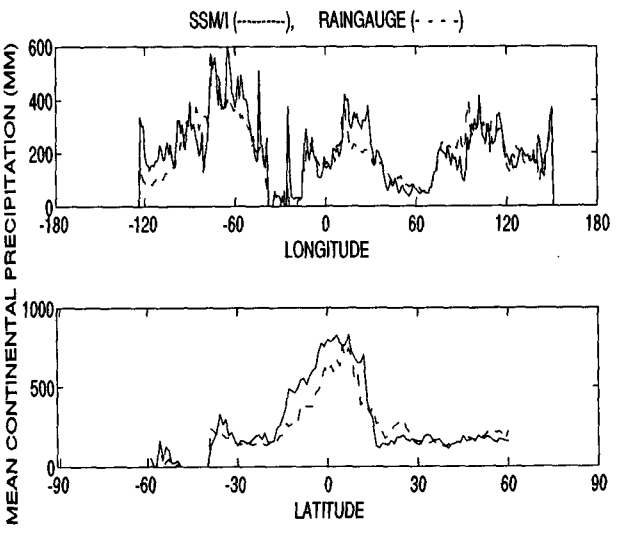

FIG. 13. Zonally and meridionally averaged distributions of total global continental precipitation for August through November 1987 from estimates by the SSM/I algorithm and a rain gauge average by the GPCC.

TABLE 3. Statistics calculated from a comparison of the SSM/I ocean algorithm and the Legates–Willmott (LW) ocean precipitation climatology. Monthly precipitation totals at 1° resolution for the period August–November 1987 are compared. The LW data represent a climatological mean derived from shipboard observations, whereas the SSM/I retrievals are direct measurements for the specific time period. Statistics are calculated from matching each grid point from −180° to 180° longitude and −60° to 60° latitude. The mean of the SSM/I and LW precipitation totals are calculated as the mean of all reported precipitation totals including zeroes over ocean surfaces. The mean difference, mean absolute difference, and correlation coefficient are calculated by pairing corresponding gridded SSM/I and LW precipitation totals for all reported values over ocean surfaces.

SSM/I mean	371.7 mm
Legates and Willmott mean	440.0 mm
Mean difference	−68.3 mm
Mean absolute difference	217.8 mm
Correlation coefficient	0.71

analyzed in Fig. 13, where the zonal and meridional averages of the continental 4-month totals are compared. The GPCC shows less high-frequency variability along both latitude and longitude, which may be the result of the rain gauge interpolation technique. The two datasets are closely correlated over both latitude and longitude; the only distinguishable difference occurs between −20° and 0° latitude where the SSM/I algorithm is approximately 50–100 mm higher than the GPCC.

The Legates and Willmott (LW) ocean climatology comparison results are listed in Table 3. The SSM/I mean for the 4-month totals is 371.7 mm and the LW mean is 440.0 mm yielding a difference of (SSM/I − LW) = −68.3 mm. The mean absolute difference is 217.8 mm and the correlation coefficient is 0.71. It is expected that the SSM/I should estimate precipitation more accurately over oceans than over land because of the cold polarized background provided by the ocean surface. The reason that the correlation is not higher than over land is probably because the LW represents a climatological mean, whereas the SSM/I data were collected during the particular period in 1987, which also corresponds to an El Niño–Southern Oscillation (ENSO) event.

Histograms for the LW–SSM/I comparison shown in Fig. 14 provide an explanation for the higher estimates from LW. The LW precipitation totals are lognormally distributed, whereas the SSM/I totals are logarithmically distributed. The lognormal LW distribution is unlike the logarithmic distributions exhibited by SSM/I over land and ocean or the distribution of GPCC over land. An examination of the zonal and meridional averages in Fig. 15 determines that the higher LW estimates are located south of −10° latitude and west of −70° longitude in the South Pacific Ocean. The 4-month comparisons for both land and oceans verify that the SSM/I algorithm closely agrees with surface-based precipitation retrievals when global estimates at spatial scales of 1° are desired.

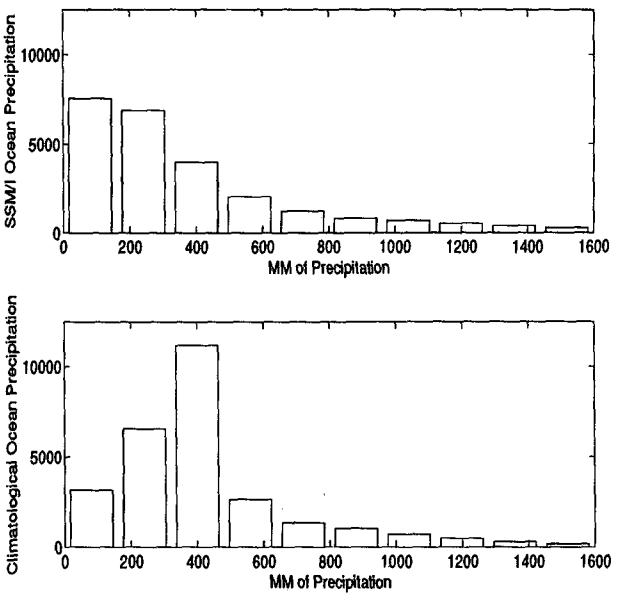

FIG. 14. Distributions of total global oceanic precipitation for August through November 1987 from estimates by the SSM/I algorithm and a shipboard climatology by Legates and Willmott.

5. Conclusions

An algorithm for estimating precipitation from SSM/I data is developed, implemented, and compared to independent surface observations. Well-established radiative transfer techniques are employed to model the SSM/I response to variable rain rates. An inversion scheme for converting T_b to rain rate is developed that is relatively simple to apply, globally applicable, and

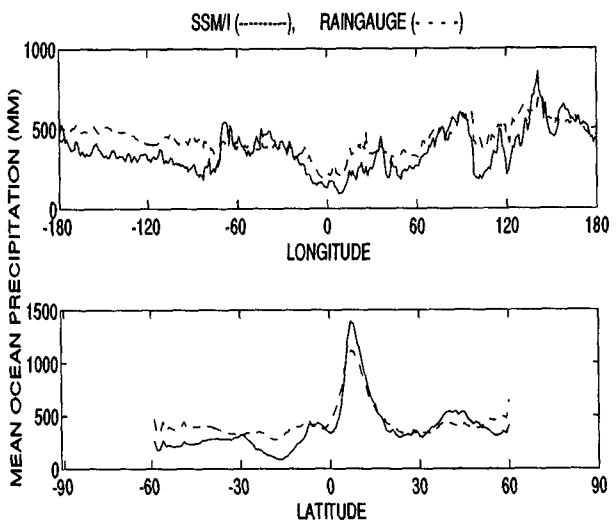

FIG. 15. Zonally and meridionally averaged distributions of total global oceanic precipitation for August through November 1987 from estimates by the SSM/I algorithm and a shipboard rain gauge climatology by Legates and Willmott.

easily calibrated. The algorithm is applicable to all SSM/I data with latitude less than 60° and with coastlines left indeterminant. The algorithm implementation can be concisely summarized. Over ocean surfaces, if $(19V - 19H) < 60$, then calculate rain rate using the equation $RR = (19H + 19V + 37H - 22V - 37V - 85H + 170.2)/18.3$ mm h^{-1}; otherwise the rain rate is set to 0 mm h^{-1}. Over land surfaces, if $(37V - 37H) < 10$ and $(19V - 19H) < 10$ and $(19V > 255)$, then calculate rain rate using the equation $RR = [19H + 37H - 2(85H) + X]/9.1$ mm h^{-1}, where $X = (-15.6 + |(\text{latitude} + \text{season offset})/5|)$ and the season offset is 20 during December, January, and February, −20 during June, July, and August, and 0 during the remaining months; otherwise the rain rate is set to 0 mm h^{-1}.

The algorithm captures both emission- and scattering-dominated rain events, exhibits a reduced beam-filling error, and operates over a variety of climatological conditions. Comparisons between the SSM/I algorithm estimates and cloud model and precipitation radar show that the differences in the instantaneous estimates are less than the mean rain rate. A 4-month global comparison to continental and shipboard rain gauge datasets confirms the validity of the algorithm with mean differences within 15% of the estimated mean and correlations of 0.7.

Acknowledgments. The helpful suggestions and valuable assistance from Wes Berg, Kelly Luetkemeyer, George Born, and Christian Kummerow are greatly appreciated. Significant improvements to the manuscript resulted from an insightful evaluation by the three reviewers. This research was sponsored in part by NASA WetNet Grant NAGW-1960, NFS Grant ATM-9023623, and in part by the U.S. Department of Energy, under appointment to the Graduate Fellowships for Global Change administered by Oak Ridge Institute for Science and Education.

REFERENCES

Adler, R. F., A. J. Negri, P. R. Keehn, and I. M. Hakkarinen, 1993: Estimation of monthly rainfall over Japan and surrounding waters from a combination of low-orbit microwave and geosynchronous IR data. *J. Appl. Meteor.*, **32,** 335–356.

Berg, W., and R. Chase, 1992: Determination of mean rainfall from the Special Sensor Microwave/Imager (SSM/I) using a mixed lognormal distribution. *J. Atmos. Oceanic Technol.*, **9,** 129–141.

Chiu, L. S., G. R. North, D. A. Short, and A. McConnell, 1990: Rain estimation from satellites: Effect of finite field of view. *J. Geophys. Res.*, **95,** 2177–2185.

Ferriday, J. G., and C. D. Kummerow, 1992: Estimating instantaneous horizontal rainfall variability from space. *Proc. Specialist Meeting on Microwave Radiometry and Remote Sensing Applications,* Boulder, CO, NOAA, 284–288.

Global Precipitation Climatology Center, 1992: Monthly precipitation estimates based on gauge measurements on the continents for the year 1987. Tech. Rep. DWD/K7/WZN-1992/08-1, World Meteorological Organization, 20 pp.

Grody, N. C., 1991: Classification of snow cover and precipitation using the Special Sensor Microwave Imager (SSM/I). *J. Geophys. Res.*, **96,** 7423–7435.

Hollinger, J., R. Lo, and G. Poe, 1987: *Special Sensor Microwave/Imager User's Guide.* Naval Research Laboratory, 120 pp.

Kummerow, C., R. A. Mack, and I. M. Hakkarinen, 1989: A self-consistency approach to improve microwave rainfall rate estimation from space. *J. Appl. Meteor.*, **28,** 869–884.

Lee, T. H., J. E. Janowiak, and P. A. Arkin, 1991: Atlas of products from the Algorithm Intercomparison Project 1: Japan and surrounding oceanic regions (June–August 1989). Tech. Rep., University Corporation for Atmospheric Research, 131 pp.

Legates, D. R., and C. J. Willmott, 1990: Mean seasonal and spatial variability in gauge-corrected, global precipitation. *Int. J. Climatol.*, **10,** 111–127.

Liou, K.-N., 1980: *An Introduction to Atmospheric Radiation.* International Geophysical Series, Vol. 26, Academic Press, 392 pp.

Liu, G., and J. A. Curry, 1992: Retrieval of precipitation from satellite microwave measurement using both emission and scattering. *J. Geophys. Res.*, **97**(D9), 9959–9974.

Olson, W. S., 1989: Physical retrieval of rainfall rates over the ocean by multispectral microwave radiometry: Application to tropical cyclones. *J. Geophys. Res.*, **94,** 2267–2279.

Smith, E. A., and A. Mugnai, 1988: Radiative transfer to space through a precipitating cloud at multiple microwave frequencies. Part II: Results and analysis. *J. Appl. Meteor.*, **27,** 1074–1091.

Spencer, R. W., B. B. Hinton, and W. S. Olson, 1983: *Nimbus-7* 37 GHz radiances correlated with radar rain rates over the Gulf of Mexico. *J. Climate Appl. Meteor.*, **22,** 2095–2099.

——, M. H. Goodman, and R. E. Hood, 1989: Precipitation retrieval over land and ocean with the SSM/I: Identification and characteristics of the scattering signal. *J. Atmos. Oceanic Technol.*, **6,** 254–273.

Tao, W.-K., J. Simpson, and S.-Y. Soong, 1987: The statistical properties of a cloud ensemble: A numerical study. *J. Atmos. Sci.*, **44,** 3175–3187.

Wilheit, T. T., 1986: Some comments on passive microwave measurement of rain. *Bull. Amer. Meteor. Soc.*, **67,** 1226–1232.

Wu, R., and J. A. Weinman, 1984: Microwave radiances from precipitating clouds containing aspherical ice, combined phase, and liquid hydrometeors. *J. Geophys. Res.*, **89,** 7170–7178.